

Article

Investigations on the Modulation Strategies for Performance Improvement of a Controlled Wind Energy System

Rajababu Durgam ¹, Ramsha Karampuri ², Shriram S. Rangarajan ^{3,4,*}, Umashankar Subramaniam ⁵ ,
E. Randolph Collins ^{4,6,*} and Tomonobu Senju ⁷ 

- ¹ Department of Electrical and Electronics Engineering, S R University, Hasanparthy, Warangal 506 371, Telangana, India
- ² Department of Electrical Engineering, Visvesvaraya National Institute of Technology, Nagpur 440011, Maharashtra, India
- ³ Department of Electrical and Electronics Engineering, Dayananda Sagar College of Engineering, Bengaluru 560078, Karnataka, India
- ⁴ Department of Electrical and Computer Engineering, Clemson University, Clemson, SC 29634, USA
- ⁵ Renewable Energy Lab, College of Engineering, Prince Sultan University, Riyadh 11586, Saudi Arabia
- ⁶ College of Engineering and Technology, Western Carolina University, Cullowhee, NC 28723, USA
- ⁷ Department of Electrical and Electronics Engineering, Senbaru, Nishihara, Nakagami District, Okinawa 903-0213, Japan
- * Correspondence: shriras@g.clemson.edu (S.S.R.); collins@clemson.edu or rcollins@wcu.edu (E.R.C.)



Citation: Durgam, R.; Karampuri, R.; Rangarajan, S.S.; Subramaniam, U.; Collins, E.R.; Senju, T. Investigations on the Modulation Strategies for Performance Improvement of a Controlled Wind Energy System. *Electronics* **2022**, *11*, 3931. <https://doi.org/10.3390/electronics11233931>

Academic Editor: Ahmed Abu-Siada

Received: 29 September 2022

Accepted: 25 November 2022

Published: 28 November 2022

Publisher's Note: MDPI stays neutral with regard to jurisdictional claims in published maps and institutional affiliations.



Copyright: © 2022 by the authors. Licensee MDPI, Basel, Switzerland. This article is an open access article distributed under the terms and conditions of the Creative Commons Attribution (CC BY) license (<https://creativecommons.org/licenses/by/4.0/>).

Abstract: The challenges faced in an isolated wind energy conversion system (WECS) are larger transient times, high steady-state error, and larger harmonic content. To overcome these issues, an adaptive voltage controller (AVC) along with the load current observer (LCO) could be the better proposition. However, the AVC and LCO, in conjunction with the conventional space vector pulse width modulation (SVPWM) technique to operate the three-phase inverter of WECS, would not be able to further improve these parameters. This paper proposes the use of the unified voltage SVPWM (UVSVPWM) technique along with the AVC and LCO, which could improve the transient behavior by about 30% as well as reduce the harmonic content of the load voltage and current by about 70% and 2%, respectively. This paper considers an isolated WECS connected to the linear load, which is operated under balanced as well as unbalanced load conditions. The proposed control technique is verified for both the balanced and unbalanced cases using MATLAB/Simulink.

Keywords: adaptive voltage controller; inverter; load current observer; renewable energy; space vector PWM

1. Introduction

Worldwide, the electrical load demand is continuously increasing due to increasing population and industry needs [1]. To supply the increasing electrical load demand and remote area electrification [2], the countries are looking toward renewable energy-based electrical power generation, such as wind and solar energy sources, because they are environmentally friendly and freely available [3,4]. Renewable energy-based distributed generation systems (DGS) has been increased in recent years to reduce global warming due to greenhouse gases emission by conventional energy sources and utilization of conventional sources such as coal, diesel, petrol, etc. [5,6]. In practice, the DGS can be operated as either a grid-connected application or a stand-alone application. When the DGS operates as grid-connected, they not only supply the required electrical power but also increase the reliability of the grid. If any fault occurs in the grid, the grid is isolated from the system, but the DGS can be operated in isolated mode, and they can supply the electricity to the local loads and improve the system reliability [7–11].

In stand-alone mode, the DGS are used to supply electricity to remote areas and/or isolated areas that are isolated from the grid. In general, the DGS are preferred to operate in

isolated mode, and they should supply the electricity to the local loads within the specified voltage and frequency range [12–17]. However, in case of large and sudden changes in the linear loads and/or non-linear loads under balanced or unbalanced conditions, controlling voltage and frequency is a challenging task. Therefore suitable controllers are required to control the terminal voltage and reduce its total harmonic distortion (THD) of a stand-alone system, specifically a wind energy conversion system (WECS).

In recent years, many types of controllers have been proposed to control the terminal voltage and frequency of an isolated DGS [18–24]. In [18,20], a robust servomechanism control theory with a discrete sliding mode current controller is used to estimate the change of voltages under sudden changes in linear or non-linear loads. This is performed to reduce the THD and to improve the transient response of the DGS. Another work reported in [21,24] again uses a robust servomechanism controller along with internal frequency control to regulate the system voltage and frequency. In this case, the system has more stability, fast transient response, and zero steady-state error.

Later in [25], the direct iterative learning controller scheme is proposed to achieve improved steady-state performance with very low errors. Using this controller, the dynamic response of the system is not so suitable under sudden change in the load. So, a modified proportional and derivative (PD) controller is connected in parallel to iterative learner, which could improve the dynamic response. However, the controller has many loops, which increases the complexity of the system and response time.

A closed-loop feed-forward voltage compensation system was proposed in [26] to regulate the voltage and frequency of a DGS. In addition, a predictive controller has been designed to forecast the voltage and current under linear load variations [27]. However, it is not suitable for sudden and large changes in loads. To overcome this issue, a steepest descent digital adaptive algorithm is used for the design of a modified stationary frame predictive current controller with zero steady-state error for DGS [28]. In this, a multi-loop control technique is proposed, which increases the complexity of the system.

The theory of adaptive voltage control [29] was used in [30] to improve the transient response and to reduce the harmonics in the voltage and current in a WECS. This system also shows better dynamics under balanced and unbalanced load conditions. The system proposed in [30,31] uses load current observer (LCO) and adaptive voltage controller (AVC) along with the conventional space vector pulse width modulation (SVPWM) technique [32]. The AVC is employed to regulate the system voltage and frequency, which uses the data of inverter and load voltages and currents. The voltages and currents were measured using sensors and fed to the AVC. However, the use of more sensors leads to slow response and complexity of the system. Hence, the LCO is used to estimate the load currents, thereby eliminating the sensors. The three-phase inverter is operated using the conventional SVPWM technique, which acquires reference data from the AVC.

However, there is still scope for improvement in the transient response and reduce the harmonic content. This could be achieved by utilizing unified voltage SVPWM (UVSVPWM) [32–35] in place of the conventional SVPWM technique. Hence, this paper proposes UVSVPWM in conjunction with the AVC and LCO to reduce the transient response time of the WECS under sudden load change conditions; also, to reduce the THD of the load voltage and current of the WECS.

Rest of the paper is divided into five sections, wherein the Section 2 describes the system considered, Section 3 elaborates the controller design. Sections 4 and 5 depict the simulation and experimental results, respectively. Section 6 concludes the work presented in this paper.

2. Mathematical Model of the System

The schematic circuit diagram of the system is shown in Figure 1. It consists of WECS along with the rectifier, a three-phase inverter, inductive and capacitive (LC) filter, controller, and local load. This paper mainly deals with the design of voltage controller to regulate the load voltage under steady state and dynamic loaded conditions. Hence, the energy

conversion system from renewable energy resources, i.e., WECS and the converter can be replaced by DC voltage source as emulated by two dc-link capacitors viz. $C/2$. In Figure 1, the inverter is used to convert DC to AC and the variations in the output voltage and frequency can be obtained using suitable pulse width modulation (PWM) technique. The LC filter is used to reduce the higher order harmonics in the output power of the inverter. After elimination of the harmonics and making the power nearly sinusoidal, the supply is given to the local load. The work presented in this paper is limited to linear load. However, the proposed system and controller can be extended to non-linear loads either. The mathematical modeling of all the components of the system shown in Figure 1 is briefly explained below for the use of simulation studies.

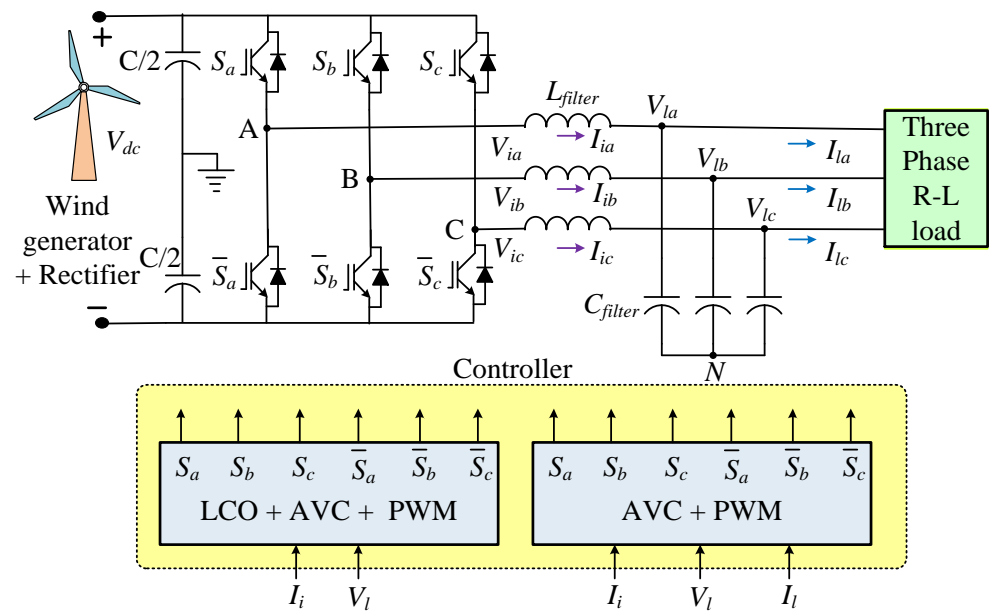


Figure 1. Schematic circuit diagram of the wind energy conversion system.

The DC-bus voltage is considered to be V_{dc} . The inverter is operated using a specific PWM technique that generates the firing pulses, which can be represented by the switching functions S_a , S_b , and S_c for three phases, a, b, and c, respectively. The inverter output voltages and currents are represented by V_{ia} , V_{ib} , V_{ic} and I_{ia} , I_{ib} , I_{ic} , respectively, whereas the load voltages and currents are represented as V_{la} , V_{lb} , V_{lc} and I_{la} , I_{lb} , I_{lc} , respectively. The inverter output voltages can be represented by using the switching functions:

$$V_{ia} = \frac{V_{dc}}{2} \left[\frac{2}{3}S_a - \frac{1}{3}(S_b + S_c) \right] \tag{1}$$

$$V_{ib} = \frac{V_{dc}}{2} \left[\frac{2}{3}S_b - \frac{1}{3}(S_c + S_a) \right] \tag{2}$$

$$V_{ic} = \frac{V_{dc}}{2} \left[\frac{2}{3}S_c - \frac{1}{3}(S_a + S_b) \right] \tag{3}$$

Applying Kirchhoff’s laws at the filter nodes to obtain the voltage and current equations as follows:

$$\begin{bmatrix} dV_{ia}/dt \\ dV_{ib}/dt \\ dV_{ic}/dt \end{bmatrix} = \frac{1}{C_{filter}} \begin{bmatrix} I_{ia} - I_{la} \\ I_{ib} - I_{lb} \\ I_{ic} - I_{lc} \end{bmatrix} \tag{4}$$

$$\begin{bmatrix} dI_{ia}/dt \\ dI_{ib}/dt \\ dI_{ic}/dt \end{bmatrix} = \frac{1}{L_{filter}} \begin{bmatrix} V_{ia} - V_{la} \\ V_{ib} - V_{lb} \\ V_{ic} - V_{lc} \end{bmatrix} \tag{5}$$

The above Equations (4) and (5) can be transformed into stationary reference frame ($\alpha\beta$) and then synchronously rotating reference frame (dq). The transformed dq quantities can be used in implementing LCO and AVC. The derived dq quantities can be written as follows:

$$\frac{dV_{ld}}{dt} = \omega V_{lq} + \frac{1}{C_{filter}}(I_{ld} - I_{ld}) \tag{6}$$

$$\frac{dV_{lq}}{dt} = -\omega V_{ld} + \frac{1}{C_{filter}}(I_{lq} - I_{lq}) \tag{7}$$

$$\frac{dI_{id}}{dt} = \omega I_{iq} + \frac{1}{L_{filter}}(V_{id} - V_{ld}) \tag{8}$$

$$\frac{dI_{iq}}{dt} = -\omega I_{id} + \frac{1}{L_{filter}}(V_{iq} - V_{lq}) \tag{9}$$

Equations (6)–(9) resemble state-space equations wherein the parameters V_{ld} , V_{lq} , I_{id} , and I_{iq} are the state variables; V_{id} and V_{iq} are taken as control inputs; and I_{ld} and I_{lq} are considered to be disturbances.

3. Detailed Description and Design of Controllers

The system shown in Figure 1 is controlled using AVC. The input parameters required to implement AVC are: inverter output current (I_i), load voltage (V_l), and load current (I_l). The load current to the AVC can be fed either directly from the sensors or through the LCO. The LCO can be used to improve the transient behavior of the system.

3.1. Adaptive Voltage Controller

The AVC can be designed using reference adaptive control theory. It depends on the existing reference model that brings out the desired performance of the voltage control scheme. The block diagram of AVC is shown in Figure 2. The inputs given to the AVC are the transformed dq-axis parameters from the sensed values of inverter current, load current, and load voltages, along with the generated reference load voltages. All the given signals are processed using Equations (10)–(15) to obtain the desired reference dq-axis voltage signals for the PWM algorithm.

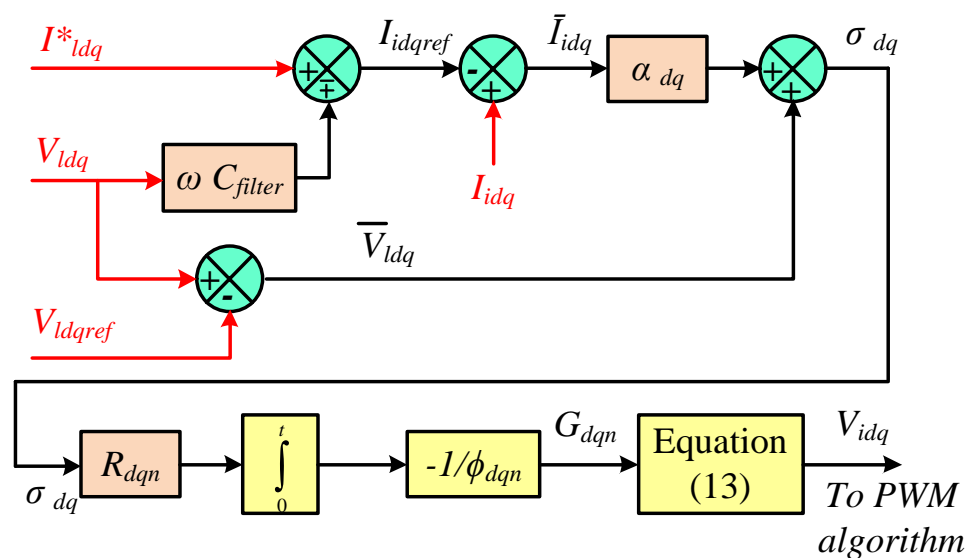


Figure 2. Block diagram for the implementation of adaptive voltage controller.

The inverter output reference currents before the filter are represented as:

$$I_{idq\ ref} = I_{dq}^* \mp \omega C_{filter} V_{lq} \tag{10}$$

where I_{dq}^* represents either I_{dq} for sensed load currents or \hat{I}_{dq} for estimated load currents using LCO, as discussed in the next subsection.

The dq-axis error in voltages after the filter is represented as:

$$\bar{V}_{dq} = V_{dq} - V_{dq\ ref} \tag{11}$$

The dq-axis error in currents before the filter is represented as:

$$\bar{I}_{dq} = I_{dq} - I_{dq\ ref} \tag{12}$$

The following adaptive control laws can be used to dq-axis compensation control parameters and feedback control parameters to stabilize the error under dynamic conditions of WECSs. The compensation control parameters can be represented in terms of adaptive gains of the dq-axis (G_{dn} and G_{qn}) as (n being the number of rows of the matrix that is equal to 4).

$$V_{dq} = \left(\sum_{n=1}^4 G_{dq_n} R_{dq_n} + V_{dq} \right) - \left(\partial_{dq} \sigma_{dq} \right) \tag{13}$$

where

$$G_{dq_n} = -\frac{1}{\phi_{dq_n}} \int_0^t R_{dq_n} \sigma_{dq} d\tau \tag{14}$$

$$R_{dq_n} = [V_{lq} \quad I_{id} \quad I_{iq} \quad 1]^T \tag{15}$$

$$\sigma_{dq} = \bar{V}_{dq} + \alpha_{dq} \bar{I}_{dq} \tag{16}$$

where α_{dq} are positive design constants and ∂_{dq} and ϕ_{dq_n} are tuned following the tuning rules provided in [36,37].

3.2. Load Current Observer

As discussed above, the AVC requires the load current data, which can be obtained either by using sensors or by estimation. However, usage of sensors leads to increased cost of the system and degrades its reliability. Hence, estimation of load currents using the available data from the inverter output voltages and inverter output currents could be the better proposition.

The estimated values of load currents (I_{dq}) required by the AVC could be obtained using the dynamic state-space model, as discussed below.

The state-space representation of Equations (6)–(9) can be performed as given in (17). From (17), the matrices X, A, B, and U can be deduced, which is in the standard state-space representation form. Using these matrices, the LCO can be designed as given in (18). In (18), the voltage and current values are the estimates of load voltages and currents.

$$\begin{bmatrix} \dot{\hat{X}} \\ \hat{I}_{ld} \\ \hat{I}_{lq} \\ \hat{V}_{ld} \\ \hat{V}_{lq} \end{bmatrix} = \begin{bmatrix} 0 & 0 & 0 & 0 \\ 0 & 0 & 0 & 0 \\ -1/C_{filter} & 0 & 0 & -\omega \\ 0 & -1/C_{filter} & -\omega & 0 \end{bmatrix} \begin{bmatrix} \hat{I}_{ld} \\ \hat{I}_{lq} \\ \hat{V}_{ld} \\ \hat{V}_{lq} \end{bmatrix} + \begin{bmatrix} 0 & 0 \\ 0 & 0 \\ 1/C_{filter} & 0 \\ 0 & 1/C_{filter} \end{bmatrix} \begin{bmatrix} U \\ I_{dq} \end{bmatrix} \tag{17}$$

$$\dot{\hat{X}} = A\hat{X} + BU + MCX - MC\hat{X} \tag{18}$$

where

$$\hat{X} = [\hat{I}_{ld} \quad \hat{I}_{lq} \quad \hat{V}_{ld} \quad \hat{V}_{lq}]^T \tag{19}$$

Also, matrix M is the LCO gain matrix, as mentioned in [30]. The estimated values of load currents can be deduced from (19), as mentioned in (20).

$$\hat{I}_{ldq} = \begin{bmatrix} \hat{I}_{ld} \\ \hat{I}_{lq} \end{bmatrix} = \begin{bmatrix} 1 & 0 & 0 & 0 \\ 0 & 1 & 0 & 0 \end{bmatrix} \begin{bmatrix} \hat{I}_{ld} \\ \hat{I}_{lq} \\ \hat{V}_{ld} \\ \hat{V}_{lq} \end{bmatrix} \tag{20}$$

The deduced estimated currents can now be used as inputs to the AVC, as shown in Figure 2.

3.3. Pulse Width Modulation Techniques

The harnessed dc power from the WECS and the rectifier is converted into ac for local load utilization through an inverter. The three-phase inverter shown in Figure 1 is operated using the appropriate pulse width modulation technique to obtain the desired output power. The work proposed in [30] has used the conventional SVPWM technique, as discussed below. This paper proposes the use of the UVSVPWM technique to improve the performance of the system. Both of the PWM techniques are discussed in detail in the subsequent parts.

3.3.1. Conventional Space Vector PWM

The SVPWM technique is one of the best methods for operating the three-phase voltage source inverter (VSI) to be used in renewable energy conversion systems and AC motor drive systems [32]. The conventional way of implementing the SVPWM, either in simulation or in the experiment, is shown in Figure 3. The reference input voltages V_{id} and V_{iq} are obtained from the AVC and are processed to generate the reference voltage vector. The magnitude and angle are deduced using (21).

$$\left| \vec{V}_{ref} \right| = \sqrt{V_{\alpha}^2 + V_{\beta}^2} \text{ and } \angle \vec{V}_{ref} = \theta = \tan^{-1} \left(\frac{V_{\beta}}{V_{\alpha}} \right) \tag{21}$$

$$T_i = T_s \frac{\sqrt{3} \left| \vec{V}_{ref} \right|}{V_{dc}} \sin \left[60 - \theta - \left(\frac{N-1}{3} \right) \pi \right];$$

$$T_{ii} = T_s \frac{\sqrt{3} \left| \vec{V}_{ref} \right|}{V_{dc}} \sin \left[\theta - \left(\frac{N-1}{3} \right) \pi \right];$$

$$T_z = T_s - T_i - T_{ii}$$
(22)

where T_s is the switching time.

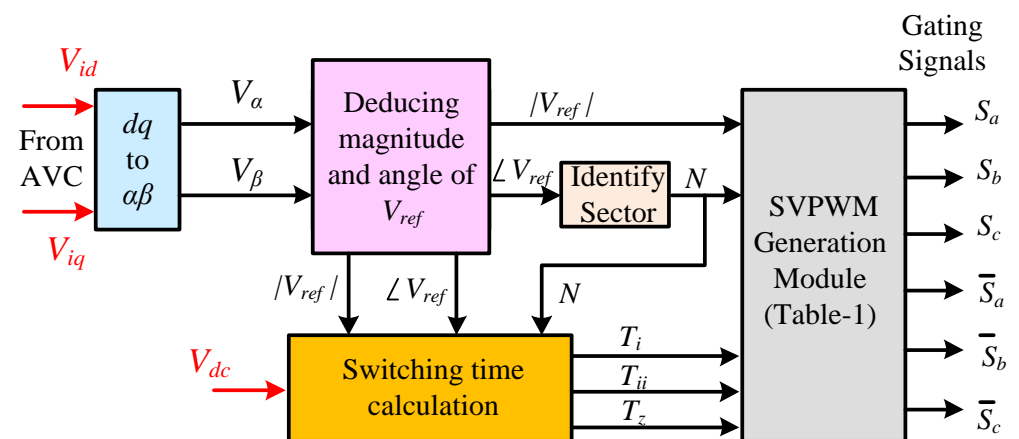


Figure 3. Block diagram for the implementation of the Conventional space vector pulse width modulation Technique.

Then using the angle information, the sectors are identified and divided into six equal parts as $N = 1$ to 6. Now, the switching times are calculated for each sector as given in (22). Then these switching times are used to realize the proper gating pulse as per given Table 1, which varies with the sector number.

Table 1. Switching time at each sector.

Sector Number	Switching Time of Upper Switches S_a, S_b, S_c	Switching Time of Lower Switches $\bar{S}_a, \bar{S}_b, \bar{S}_c$
1	$S_a = T_i + T_{ii} + T_z/2$ $S_b = T_{ii} + T_z/2$ $S_c = T_z/2$	$\bar{S}_a = T_z/2$ $\bar{S}_b = T_i + T_z/2$ $\bar{S}_c = T_i + T_{ii} + T_z/2$
2	$S_a = T_i + T_z/2$ $S_b = T_i + T_{ii} + T_z/2$ $S_c = T_z/2$	$\bar{S}_a = T_{ii} + T_z/2$ $\bar{S}_b = T_z/2$ $\bar{S}_c = T_i + T_{ii} + T_z/2$
3	$S_a = T_z/2$ $S_b = T_i + T_{ii} + T_z/2$ $S_c = T_{ii} + T_z/2$	$\bar{S}_a = T_i + T_{ii} + T_z/2$ $\bar{S}_b = T_z/2$ $\bar{S}_c = T_i + T_z/2$
4	$S_a = T_z/2$ $S_b = T_i + T_z/2$ $S_c = T_i + T_{ii} + T_z/2$	$\bar{S}_a = T_i + T_{ii} + T_z/2$ $\bar{S}_b = T_{ii} + T_z/2$ $\bar{S}_c = T_z/2$
5	$S_a = T_{ii} + T_z/2$ $S_b = T_z/2$ $S_c = T_i + T_{ii} + T_z/2$	$\bar{S}_a = T_i + T_z/2$ $\bar{S}_b = T_i + T_{ii} + T_z/2$ $\bar{S}_c = T_z/2$
6	$S_a = T_i + T_{ii} + T_z/2$ $S_b = T_z/2$ $S_c = T_{ii} + T_z/2$	$\bar{S}_a = T_z/2$ $\bar{S}_b = T_i + T_{ii} + T_z/2$ $\bar{S}_c = T_{ii} + T_z/2$

3.3.2. Unified Voltage Space Vector PWM

Despite the advantages of conventional SVPWM, such as better DC-bus utilization, lower THDs in inverter output voltage and current, and low switching losses, this PWM technique has few drawbacks. The drawbacks of the conventional SVPWM technique are: location identification of the reference vector, predetermining the nearest active voltage vectors, and, based on the vector information calculating the switching times. In other words, the conventional SVPWM uses a look-up table for its implementation. So, it is observed that in practical implementation conventional SVPWM technique is more complex and requires more time for the calculation of switching times because of trigonometric functions.

However, in the UVSVPWM technique [33], the switching time of each inverter arm can be calculated directly using the concept of the effective time period to realize the voltage vector. In this PWM technique, an exact switching pattern can easily be implemented, and the execution time and space required on the processor can be reduced.

The UVSVPWM technique is implemented, as shown in Figure 4. This technique requires the same input as in the case of conventional SVPWM, i.e., inverter voltage reference, V_{idq} , which could be obtained from AVC. Then the three-phase reference voltage waveforms are generated using standard transformation. Later the imaginary switching times are calculated, as shown in Figure 4. The maximum and minimum values from these imaginary switching times were extracted to calculate the effective time period (which is defined as the difference between the maximum and minimum times). The effective time is used to know the offset time required to add it to the imaginary times, such that those times turn into reality and can generate the switching pulses by comparing them with the generated carrier waveform. The UVSVPWM helps the WECS improve its transient time and hence its performance, which is discussed in the subsequent sections.

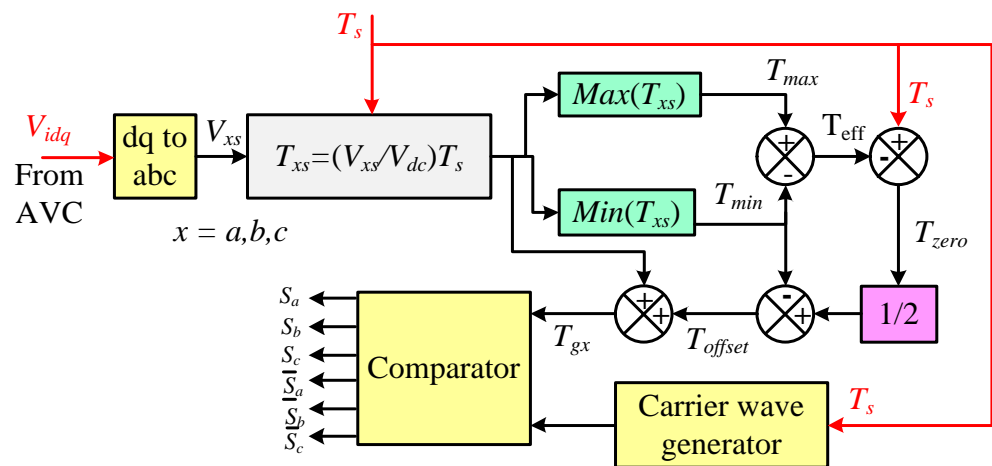


Figure 4. Block diagram for the implementation of the UVSVPWM technique.

4. Simulation Studies

In this section, the simulation results of WECS shown in Figure 1 are presented using MATLAB/Simulink. The mechanical input to the system (wind energy), the electrical energy generator, and the ac-dc converter together are emulated using a regulated dc power source, V_{dc} , whose value is set to 564 V (so as to attain the inverter output voltage to be 230 Vrms). The three-phase inverter, shown in Figure 1, is connected to the LC filter with the designed parameters of inductance, $L_{filter} = 0.3$ mH/phase and capacitance, $C_{filter} = 500$ μ F/phase. The filter output is connected to the linear resistive and inductive loads, whose values are considered to be $R_1 = 0.726$ Ω /phase and $L_1 = 0.3$ mH/phase.

The system shown in Figure 1 is tested with two different load conditions viz. balanced three-phase and unbalanced three-phase linear loads. These two conditions are simulated by connecting a three-phase circuit breaker between the filter and the load. To realize the balanced load operation, the circuit breaker is kept open from time 0 to 0.1 s. Later, all three phases of the circuit breaker are closed. The second part of the simulation considers unbalanced load operation, which is realized by closing only two phases (say b and c phases) of the three-phase circuit breaker at the same time as above, i.e., phase-a is considered to be open completely.

The three-phase inverter shown in Figure 1 is operated using the conventional SVPWM technique and the proposed UVSVPWM techniques. In addition, the considered system is operated using the AVC and the LCO in conjunction with the modulation techniques individually. The simulation is carried out in four different cases, viz. case-I, II, III, and IV, as mentioned below. In each case, the simulation results are analyzed to determine the time response of the controller and the THD of load voltage and load current.

Case-I: AVC + Conventional SVPWM

Case-II: LCO + AVC + Conventional SVPWM

Case-III: AVC + UVSVPWM

Case-IV: LCO + AVC + UVSVPWM

Figures 5–12 show the simulation results of WECS. Each figure show the waveforms of load voltages (V_{Iabc}), current waveforms from LCO (\hat{I}_{Idq}), voltage waveforms from AVC (V_{Idq}) and the measured load currents (I_{Iabc}) from top to bottom, respectively. The bottom two plots show the harmonic spectrum of load voltage and load current (say phase-b, since phase-a is considered to be open under unbalanced condition).

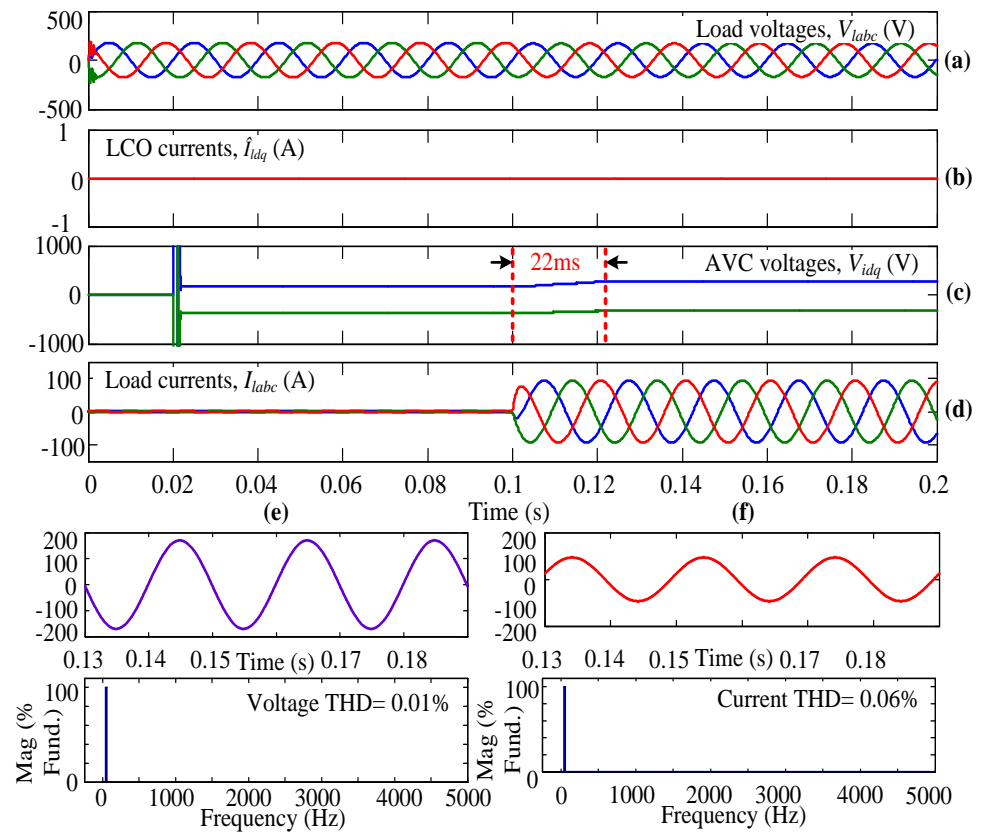


Figure 5. Simulation results for case-I with balanced load condition.

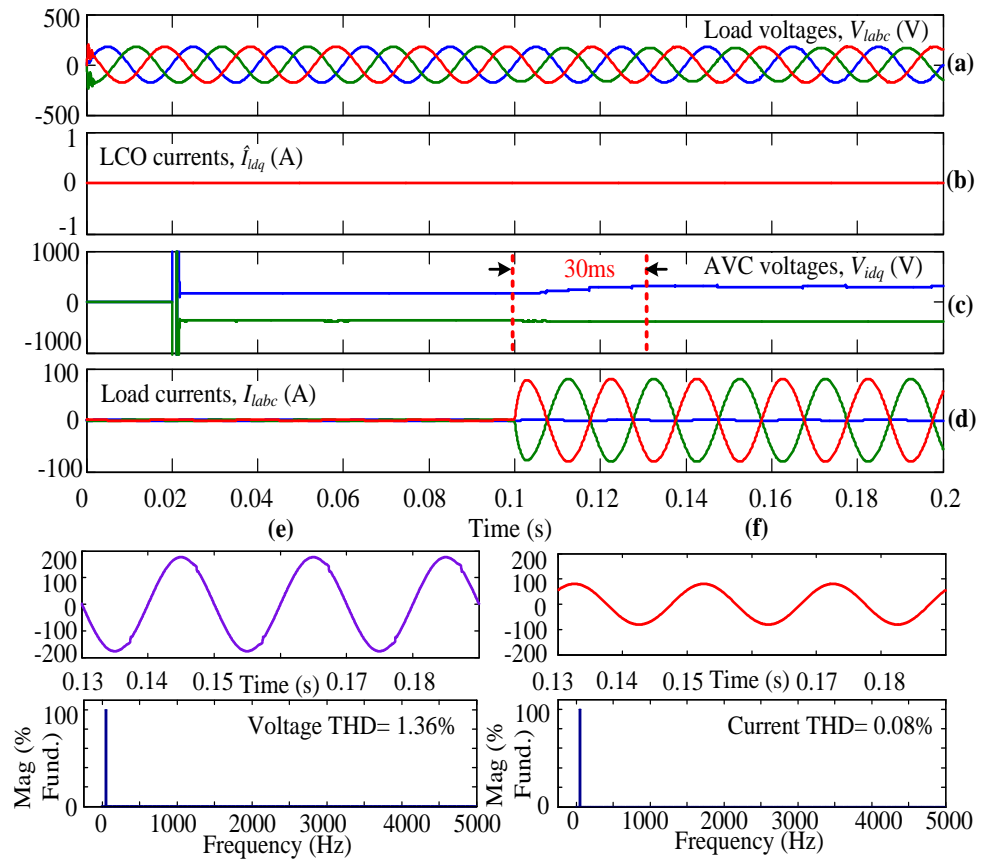


Figure 6. Simulation results for case-I with unbalanced load condition.

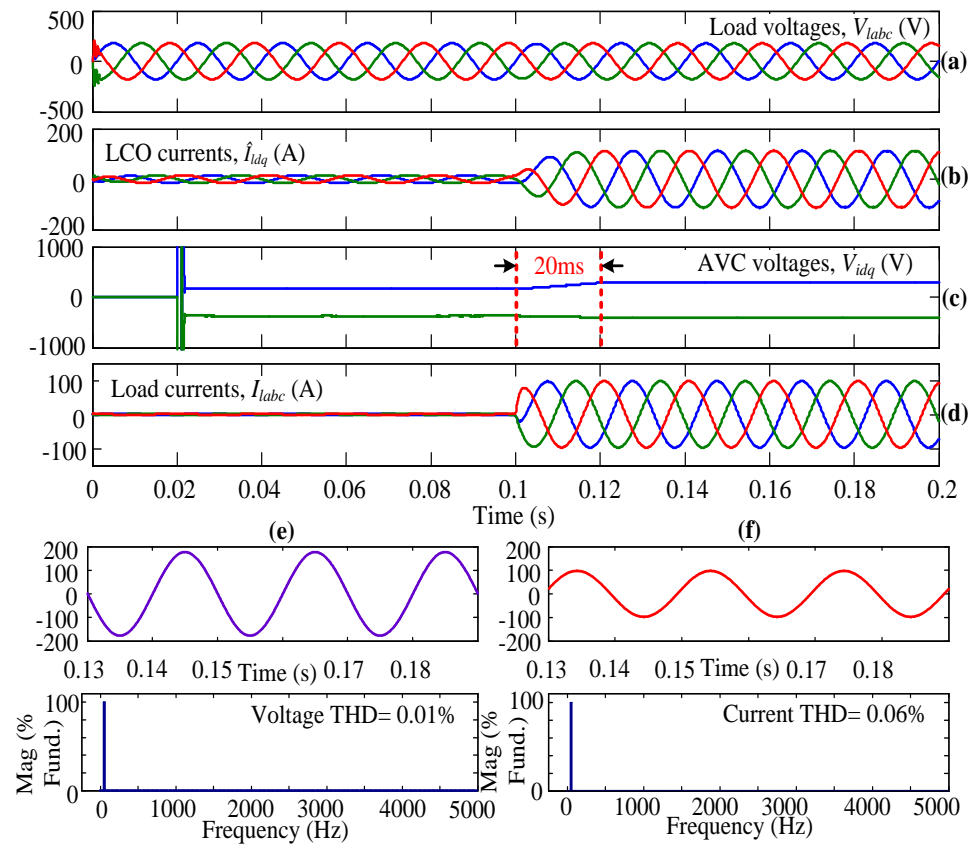


Figure 7. Simulation results for case-II with balanced load condition.

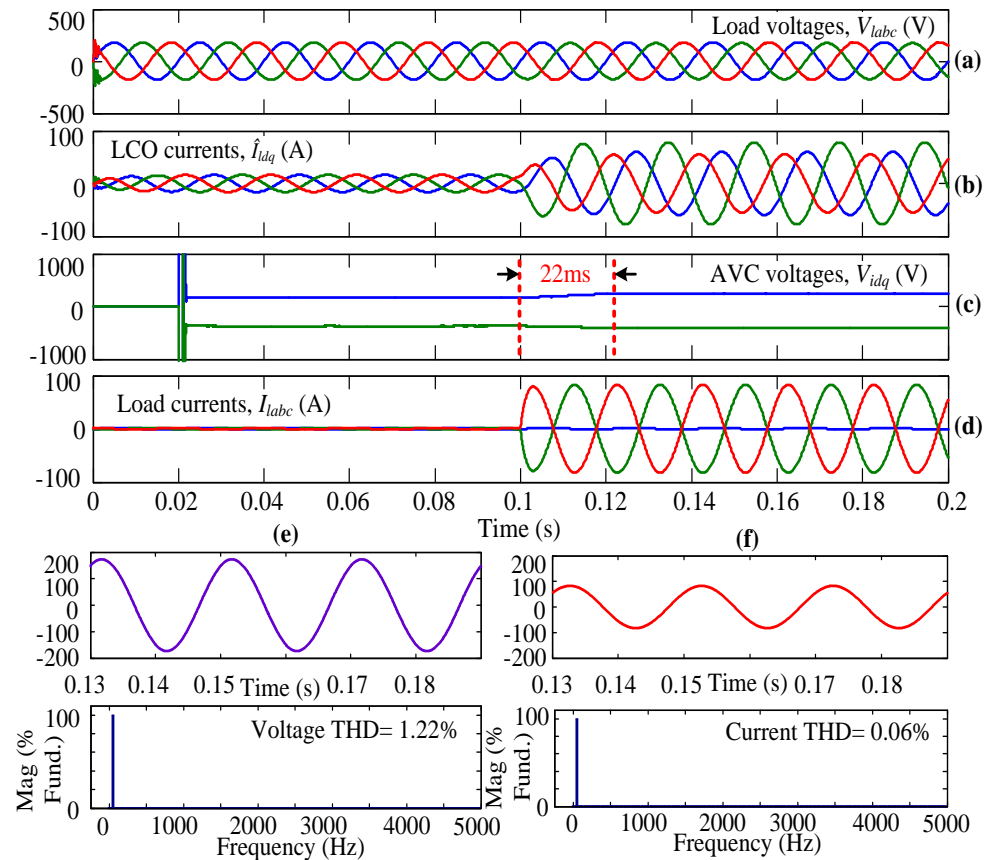


Figure 8. Simulation results for case-II with unbalanced load condition.

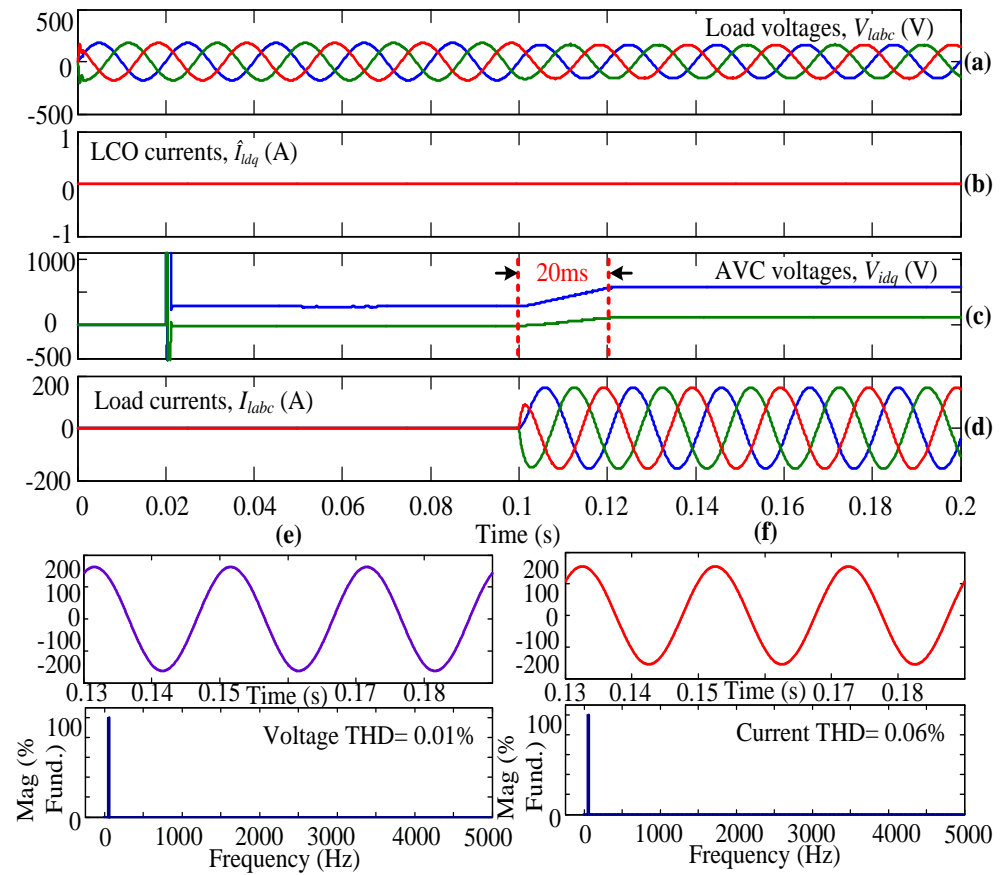


Figure 9. Simulation results for case-III with balanced load condition.

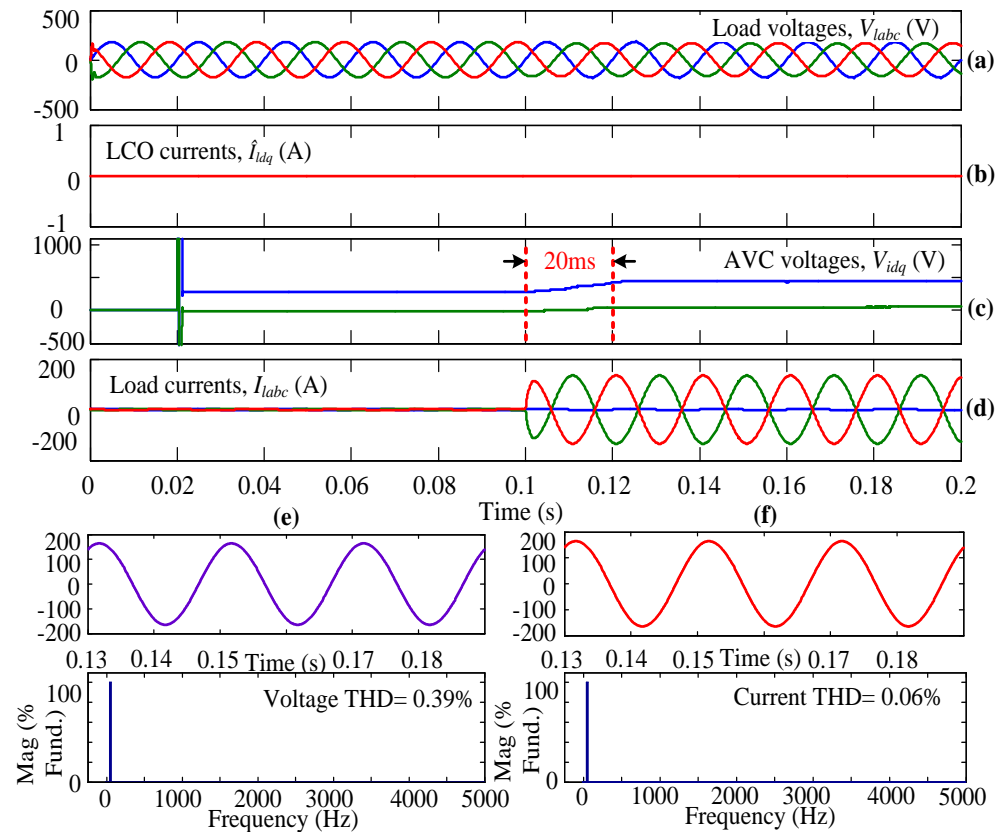


Figure 10. Simulation results for case-III with unbalanced load condition.

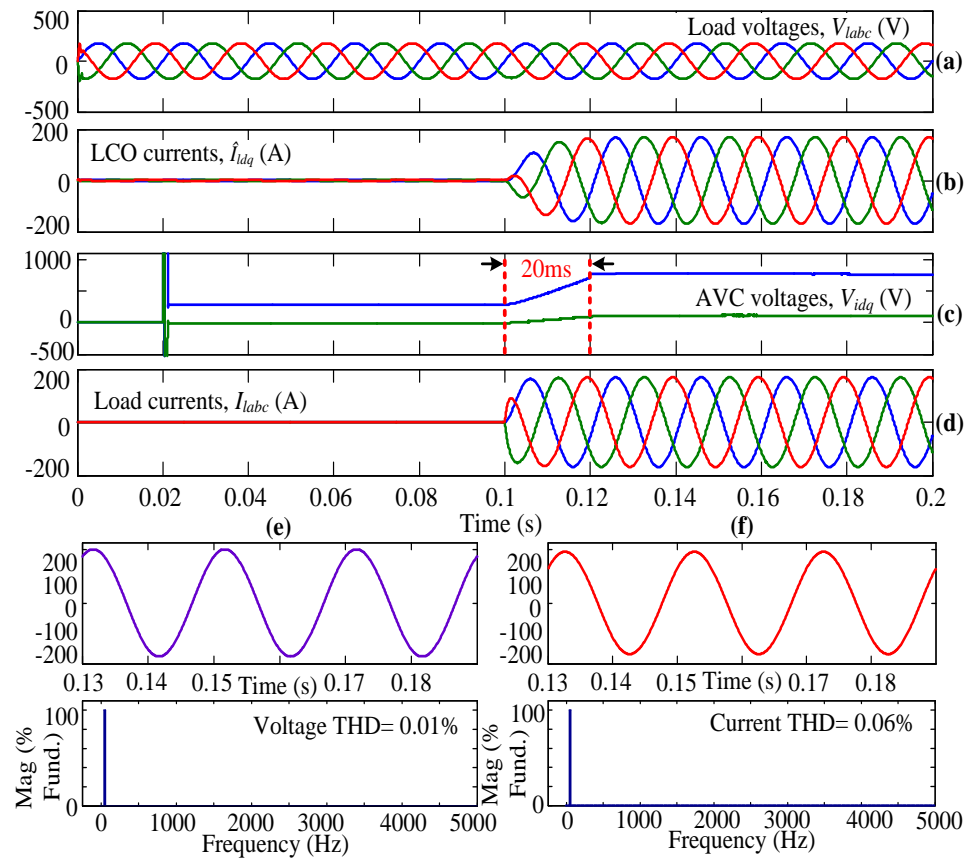


Figure 11. Simulation results for case-IV with balanced load condition.

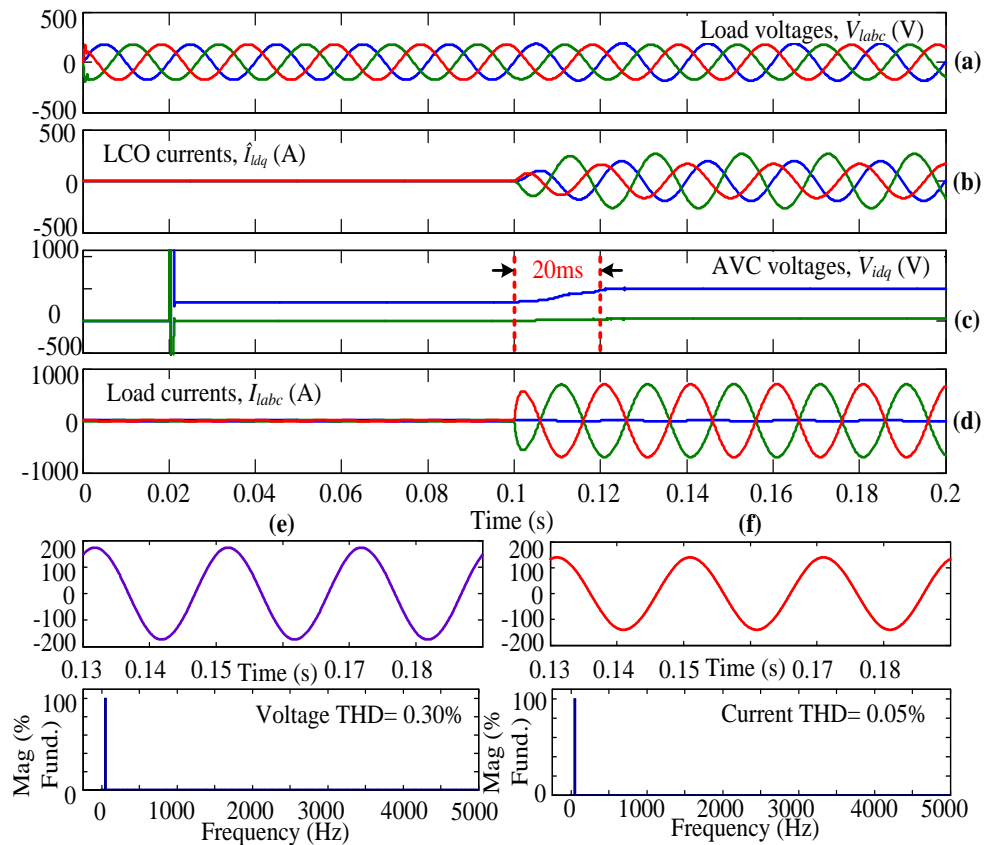


Figure 12. Simulation results for case-IV with unbalanced load condition.

4.1. Case-I

Initially, the system is simulated using AVC only but not the LCO, and the inverter is operated using the conventional SVPWM technique. In Figure 5, Figure 5a represents the three-phase load voltages that are captured after the LC filter but before the circuit breaker. Figure 5b gives the dq-axis currents from the LCO. In this subplot, it can be observed that the dq-axis currents are equal to zero because this case is simulated without LCO. When the three-phase load is connecting to the WECS using the circuit breaker (in other words, when the circuit breaker is closed), the AVC senses the load parameters and takes necessary action, which can be observed from the dq-axis voltages as shown in Figure 5c. From this plot, it can be observed that at $t = 0.1$ s, the AVC is ready to take the necessary action to obtain a steady-state load current within a few milliseconds. Figure 5d shows the load currents flowing through the three-phase linear load. From the plot, it can be seen that from time $t = 0$ s to 0.1 s, the load currents are equal to zero because the three-phase circuit breaker is kept open, so no current flows through the load. At $t = 0.1$ s, the circuit breaker is closed completely (i.e., in all three phases), and the corresponding load currents flow through the connected linear load. From Figure 5c,d, it can be observed that the system is reaching a steady state at $t = 0.12$ s because of only AVC action. The V_{id} and V_{iq} or load currents are reaching a steady state within 20 ms. From the results, the THD value of the load voltage and load current under steady-state condition, i.e., from 0.13 s, is obtained as 0.01% and 0.06%, respectively, as shown in Figure 5e,f.

The same system is also simulated with an unbalanced linear load, i.e., one of the phases (say phase-a) of the three-phase circuit breaker is kept open continuously, and the simulation results are shown in Figure 6. From Figure 6d, it can be observed that the phase-a current is equal to zero. In addition, the AVC takes necessary action, and the system approaches near steady-state. However, without using the LCO, the steady-state results are not convincing for unbalanced load conditions with conventional SVPWM, as seen in Figure 6d. The THD values of load voltage and load current for phase-b are obtained as 1.36% and 0.08%, respectively, as shown in Figure 6e,f.

4.2. Case-II

In this case, the system is simulated with AVC along with the LCO, and the inverter is operated using the same conventional SVPWM technique, and the simulation results are shown in Figures 7 and 8 for balanced and unbalanced load conditions, respectively [38]. All the results are similar to the results of case-I, except the current waveforms from the LCO, as shown in the second subplots of Figures 7 and 8. In this case, the load current reaches the steady state within a few milliseconds, and the response is faster as compared to case-I for both the balanced and unbalanced loads. The faster response is because of the use of LCO in conjunction with the AVC [30]. The harmonic spectra of respective load voltage and current are also shown in the plots, along with their THD values.

4.3. Case-III

In this case, the same WECS is simulated only by considering AVC but not the LCO, and the inverter is now operated with the UVSVPWM technique under balanced and unbalanced linear loads. The simulation results with a balanced load are shown in Figure 9, and for unbalanced load is shown in Figure 10. Similar conditions are considered as in case-I and case-II. The major advantage of using the UVSVPWM technique can be depicted by the faster and more precise action of AVC without LCO, as shown in Figure 10c (when compared to Figure 6c). All the respective harmonic spectra and THD values are shown in the last subplots for both the balanced and unbalanced load conditions.

4.4. Case-IV

In this case, the WECS is simulated using AVC along with LCO, and the inverter is operated with the UVSVPWM technique. In this case, also, the system is simulated with balanced and unbalanced linear loads [38]. Similar conditions that are considered

in the above three cases are considered, and the simulation results obtained as shown in Figure 11 with a balanced load and Figure 12 with an unbalanced load. These results show no difference in the waveforms with respect to transient and steady-state behavior; however, the use of LCO along with the UVSVPWM technique helps in reducing the THD values of load voltage and current.

All the numerical values of the above-discussed simulation results are tabulated in Table 2. The THD values of load voltage and load current, along with the transient times, are presented. The THD values are calculated by considering three cycles of the fundamental waveform. The transient time is measured from the instant when the circuit breaker is closed. The THD gives information about total harmonic content, but it does not indicate the level of each harmonic component. If a filter is used at the output of the inverter, the predominant harmonics corresponding to the designed value of the filter would be attenuated more effectively. Therefore, knowledge of both the magnitude and frequency of each harmonic is important. The distortion factor (DF) indicates the amount of harmonic distortion that remains in a particular waveform after the harmonics of the waveform have been subjected to a second-order attenuation (i.e., divided by n^2).

Table 2. Summary of simulation results.

	S. No.	Case	Type of Load	Voltage THD (%)	Distortion Factor (%)	Current THD (%)	Transient Time (ms)
Con. SVPWM	1	I}	Balanced	0.01	99.99	0.06	22
	2		Unbalanced	1.36	59.23	0.08	30
	3	II}	Balanced	0.01	99.99	0.06	20
	4		Unbalanced	1.22	63.39	0.06	22
UVSV PWM	5	III}	Balanced	0.01	99.99	0.06	20
	6		Unbalanced	0.39	93.16	0.06	20
	7	IV}	Balanced	0.01	99.99	0.06	20
	8		Unbalanced	0.30	95.78	0.05	20

The DF of an individual (n th) harmonic component can be defined as

$$DF = \frac{V_{0n}}{V_{01} \times n^2} \quad (23)$$

The distortion factor calculated using the THD data is furnished in Table 2. The distortion factor in the voltage is seen to be the same for both PWM techniques under balanced load conditions. However, under unbalanced load conditions, the UVSVPWM could be proved to be effectively superior to the conventional SVPWM technique. Hence from Table 2, it can be concluded that the proposed AVC, along with the UVSVPWM technique, yields better results with respect to the transient time, THD, and distortion factor of voltage.

5. Experimental Studies

An experimental prototype is developed to implement the proposed system, as shown in Figure 13. A 3-phase, 400 V, 50 Hz AC supply is connected to the three-phase rectifier through a 3-phase autotransformer. The regulated DC voltage is obtained from the output of the rectifier, and the regulated DC voltage is given to the input of the three-phase voltage source inverter. The inverter is used to convert regulated DC voltage to AC voltage with constant voltage and frequency, which is supplied to the RL load. An LC filter with an inductance of 15 mH and capacitance of 10 μ F is connected between the inverter and the load. The phase currents and voltages are measured in an oscilloscope, and the currents are sensed by the current sensors LEM LA-25NP whereas the voltages are sensed using LEM LV-25-P transducers. The computing signals and load currents and voltages are given to dSPACE1104 controller to generate the gate signals. Practically, the electrical loads are not constant. The change in load currents can be sensed by the sensors, and the information send to the controller when LCO is not used.

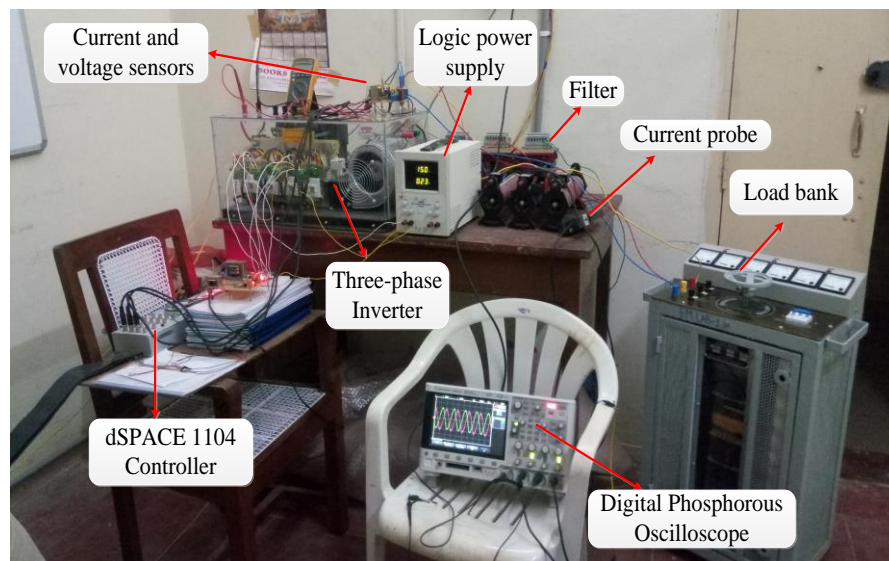


Figure 13. Experimental test rig.

Figures 14–16 show the experimental results captured from the oscilloscope as well as the dSPACE control desk. The experimental test rig is operated with the conventional SVPWM and also with the UVSVPWM. However, as discussed in Section 4, the simulation results confirm that the nature of load voltages and currents will be the same irrespective of the PWM technique used. Hence, the experimental results (load voltages and currents) presented in this section are restricted to UVSVPWM. On the other hand, the major difference is in the transient time of the controller action, which is given in Figure 16 for both of the PWM techniques.

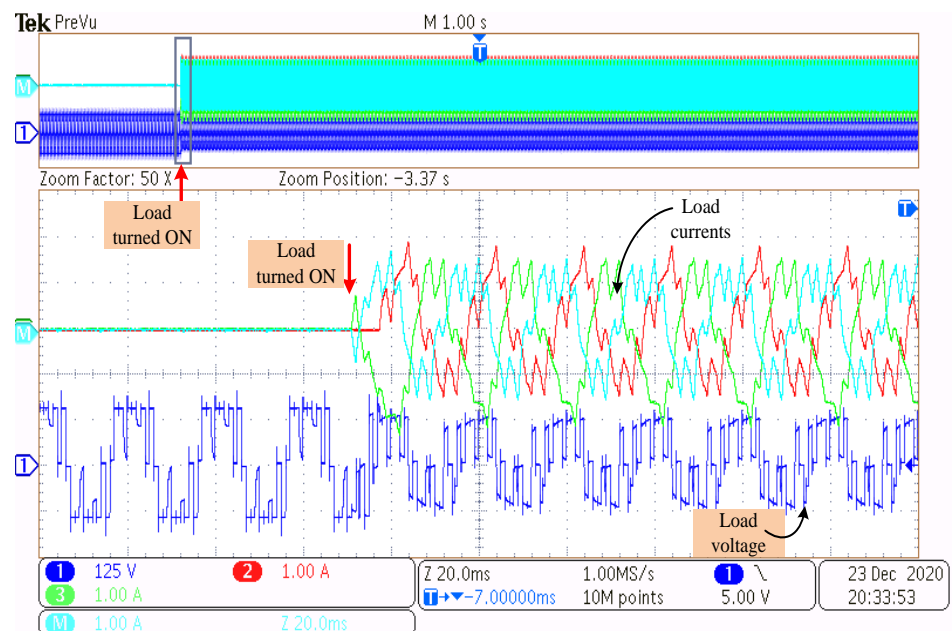


Figure 14. Experimental results using UVSVPWM under balanced load conditions.

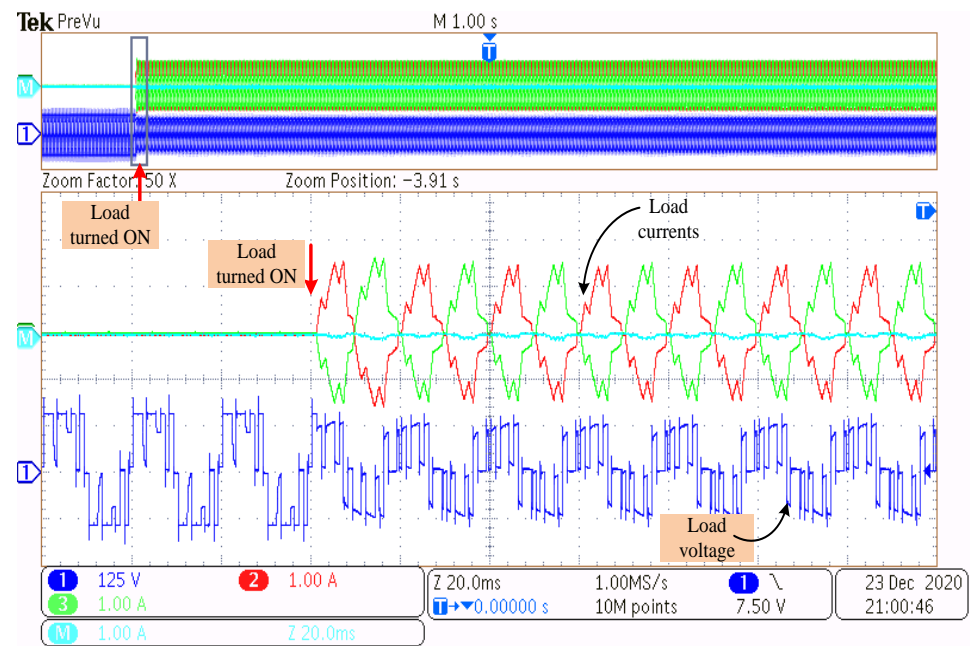


Figure 15. Experimental results using UVSVPWM under unbalanced load conditions (with one of the phases kept open).

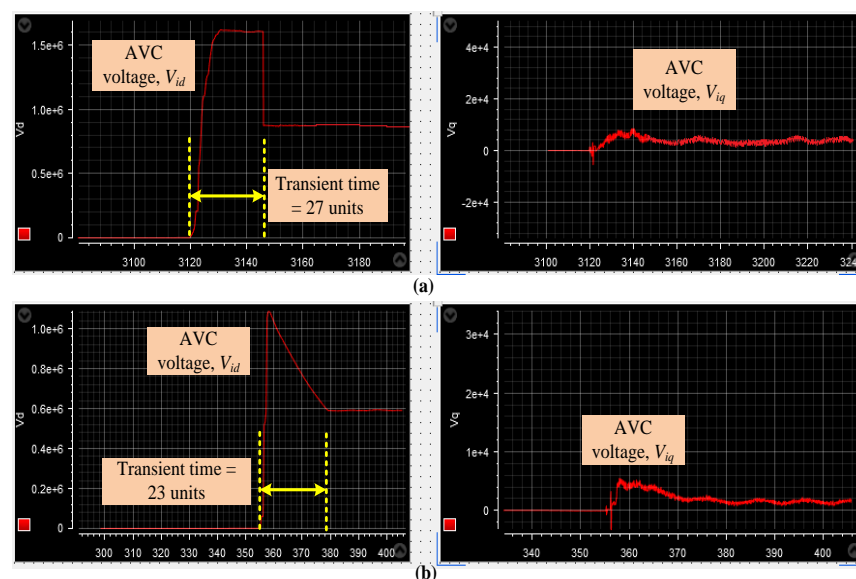


Figure 16. AVC voltages captured from dSPACE control desk (a) using conventional SVPWM (b) using UVSVPWM.

Figure 14 shows the three-phase load currents and the load voltage of one of the phases before the filter. The top plot of Figure 14 contains all the said currents and voltage, whereas the bottom plot is the zoomed view of the currents and voltage. Initially, the DC-bus voltage is applied as 150 V, and the gating pulses are generated by the controller and given to the driver circuits of the inverter without connecting any load. So, the load currents are zero until the load circuit breaker is turned ON; however, the inverter generates voltage, as seen in Figure 14. At the moment when the load circuit breaker is turned ON, the load current flows, as observed in Figure 14. Due to the unavailability of resources (such as inadequate filters) and due to the restrictions imposed (sampling frequency) by the controller, the ripple content in the phase current is very high. This ripple content can be minimized by the proper selection of filter components with respect to the switching frequency (as shown in the simulation results). However, the point of interest of this paper

is in the fast transient behavior even under unbalanced load conditions, which is shown in Figures 15 and 16.

Figure 15 shows the experimental results considering all the above conditions and are similar to Figure 14, but the only difference is in the load, i.e., one of the phases is open-circuited. So, even under unbalanced load conditions, the proposed UVSVPWM, along with the AVC, maintains the balance in the two-phase currents, as shown in Figure 15. Figure 16 depicts the transient behavior of the system using AVC voltages (direct axis–left and quadrature axis–right). When the system is operated with the conventional SVPWM technique, the transient time is seen to be 27 units (≈ 27 ms). In contrast, the transient time is observed as 23 units (≈ 23 ms) for the system operated with the UVSVPWM technique. This proves the faster dynamics of the proposed UVSVPWM along with the AVC over the conventional SVPWM technique. These plots were captured from the control desk of dSPACE, where the mathematically calculated AVC voltage signals were extracted from the controller.

6. Conclusions

The voltage and frequency control of local loads connected to the wind energy conversion system under both the balanced and unbalanced conditions is presented in this paper. For this purpose, an adaptive voltage control along with the load current observer is employed. The conventional space vector pulse width modulation technique is replaced with the unified voltage space vector pulse width modulation technique to operate the three-phase inverter. The simulation and experimental results were presented for various cases depending on the loading conditions and the controller combinations. From the presented results, it can be concluded that the use of the unified voltage space vector pulse width modulation technique could help the wind energy conversion system to reduce the transient response time by 9% to 33.3% and improve the distortion factor of the voltage for the connected linear load by 36%.

The work presented in this article is mainly based on the investigations of the PWM techniques in combination with the control techniques for an isolated wind energy conversion system consisting of various loads. However, the work can be extended to various aspects, such as the applicability of the investigated control algorithms and PWM techniques for the grid-connected wind energy system. The presented work is limited to the two-level three-phase inverter; however, the multilevel inverter connected isolated wind energy system could be studied.

Author Contributions: Conceptualization, R.D., R.K.; methodology, R.D., R.K.; software, R.D.; validation, R.D., R.K. and S.S.R.; formal analysis, R.D.; investigation, R.D., R.K., S.S.R., U.S., E.R.C. and T.S.; resources, R.K., S.S.R. and E.R.C.; data curation, R.D., R.K., S.S.R., U.S., E.R.C. and T.S.; writing—original draft preparation, R.D., R.K. and S.S.R.; writing—review and editing, R.D., R.K., S.S.R., U.S., E.R.C. and T.S.; visualization, R.D., R.K., S.S.R., U.S., E.R.C. and T.S.; supervision, R.K., S.S.R., E.R.C. and T.S.; project administration, R.D., R.K., S.S.R., U.S., E.R.C. and T.S. All authors have read and agreed to the published version of the manuscript.

Funding: This research received no external funding.

Data Availability Statement: Not applicable.

Acknowledgments: We thank NIT Warangal for providing the required facilities and the international collaborators for the research support.

Conflicts of Interest: The authors declare no conflict of interest.

References

1. Tawfiq, K.B.; Mansour, A.; Ibrahim, M.N.F.; Elkholy, E.; Sergeant, P. Implementation of matrix converter in wind energy conversion system with modified control techniques. *Electr. Power Compon. Syst.* **2019**, *47*, 1316–1331. [[CrossRef](#)]
2. Chinthamalla, R.; Karampuri, R.; Jain, S.; Sanjeevikumar, P.; Blaabjerg, F. Dual Solar Photovoltaic Fed Three-Phase Open-End Winding Induction Motor Drive for Water Pumping System Application. *Electr. Power Components Syst.* **2018**, *46*, 1896–1911. [[CrossRef](#)]

3. Djilali, L.; Sanchez, E.N.; Belkheiri, M. First and High Order Sliding Mode Control of a DFIG-Based Wind Turbine. *Electr. Power Components Syst.* **2020**, *48*, 105–116. [[CrossRef](#)]
4. Krishnamurthy, K.; Padmanaban, S.; Blaabjerg, F.; Neelakandan, R.B.; Prabhu, K.R. Power Electronic Converter Configurations Integration with Hybrid Energy Sources—A Comprehensive Review for State-of-the-Art in Research. *Electr. Power Components Syst.* **2020**, *47*, 1623–1650. [[CrossRef](#)]
5. Jha, S.K.; Kumar, D. Demand Side Management for Stand-Alone Microgrid Using Coordinated Control of Battery Energy Storage System and Hybrid Renewable Energy Sources. *Electr. Power Components Syst.* **2019**, *47*, 1261–1273. [[CrossRef](#)]
6. Ibrahim, A.M.; Attia, M.A.; Abdelaziz, A.Y. A DSM Approach for Distribution Systems with High Wind Power Penetration. *Electr. Power Components Syst.* **2020**, *48*, 56–69. [[CrossRef](#)]
7. Tu, C.-S.; Hong, C.-M.; Lu, K.-H. Design of Novel Intelligent Controller for Doubly-Fed Induction Generator-Driven Wind Turbine to Improve Transient Control Performance. *Electr. Power Components Syst.* **2020**, *48*, 174–185. [[CrossRef](#)]
8. Irfan, M.; Chandrashekhar, M.; Sushama, M. Coordinated Control of Distributed Generators and Compensator in a Micro Grid. *Int. J. Recent Technol. Eng.* **2019**, *8*, 2057–2063.
9. Ganguly, S.; Shiva, C.K.; Mukherjee, V. Frequency stabilization of isolated and grid connected hybrid power system models. *J. Energy Storage* **2018**, *19*, 145–159. [[CrossRef](#)]
10. Marwali, M.; Keyhani, A. Control of Distributed Generation Systems—Part I: Voltages and Currents Control. *IEEE Trans. Power Electron.* **2004**, *19*, 1541–1550. [[CrossRef](#)]
11. Dai, M.; Marwali, M.N.; Jung, J.-W.; Keyhani, A. A Three-Phase Four-Wire Inverter Control Technique for a Single Distributed Generation Unit in Island Mode. *IEEE Trans. Power Electron.* **2008**, *23*, 322–331. [[CrossRef](#)]
12. Karimi, H.; Davison, E.J.; Iravani, R. Multivariable Servomechanism Controller for Autonomous Operation of a Distributed Generation Unit: Design and Performance Evaluation. *IEEE Trans. Power Syst.* **2010**, *25*, 853–865. [[CrossRef](#)]
13. Karimi, H.; Yazdani, A.; Iravani, R. Robust Control of an Autonomous Four-Wire Electronically-Coupled Distributed Generation Unit. *IEEE Trans. Power Deliv.* **2011**, *26*, 455–466. [[CrossRef](#)]
14. Deng, H.; Oruganti, R.; Srinivasan, D. Analysis and Design of Iterative Learning Control Strategies for UPS Inverters. *IEEE Trans. Ind. Electron.* **2007**, *54*, 1739–1751. [[CrossRef](#)]
15. Yazdani, A. Control of an Islanded Distributed Energy Resource Unit with Load Compensating Feed-Forward. In Proceedings of the IEEE Power and Energy Society General Meeting—Conversion and Delivery of Electrical Energy in the 21st Century, Pittsburgh, PA, USA, 20–24 July 2008; pp. 1–7. [[CrossRef](#)]
16. Cortes, P.; Ortiz, G.; Yuz, J.I.; Rodriguez, J.; Vazquez, S.; Franquelo, L.G. Model Predictive Control of an Inverter With Output LC Filter for UPS Applications. *IEEE Trans. Ind. Electron.* **2009**, *56*, 1875–1883. [[CrossRef](#)]
17. Ahmed, K.H.; Massoud, A.M.; Finney, S.J.; Williams, B.W. A Modified Stationary Reference Frame-Based Predictive Current Control With Zero Steady-State Error for LCL Coupled Inverter-Based Distributed Generation Systems. *IEEE Trans. Ind. Electron.* **2011**, *58*, 1359–1370. [[CrossRef](#)]
18. Escobar, G.; Stankovic, A.; Mattavelli, P. An Adaptive Controller in Stationary Reference Frame for D-Statcom in Unbalanced Operation. *IEEE Trans. Ind. Electron.* **2004**, *51*, 401–409. [[CrossRef](#)]
19. Do, T.D.; Leu, V.Q.; Choi, Y.-S.; Choi, H.H.; Jung, J.-W. An Adaptive Voltage Control Strategy of Three-Phase Inverter for Stand-Alone Distributed Generation Systems. *IEEE Trans. Ind. Electron.* **2013**, *60*, 5660–5672. [[CrossRef](#)]
20. Manias, S.N. 6—Inverters (DC–AC Converters). In *Power Electronics and Motor Drive Systems*; Academic Press: Cambridge, MA, USA, 2017; pp. 271–500. [[CrossRef](#)]
21. Kim, J.-S.; Sul, S.-K. A Novel Voltage Modulation Technique of the Space Vector PWM. *IEEE Trans. Ind. Appl.* **1996**, *116*, 820–825. [[CrossRef](#)]
22. Karampuri, R.; Jain, S.; Somasekhar, V.T. Common-Mode Current Elimination PWM Strategy Along With Current Ripple Reduction for Open-Winding Five-Phase Induction Motor Drive. *IEEE Trans. Power Electron.* **2019**, *34*, 6659–6668. [[CrossRef](#)]
23. Åström, K.J.; Wittenmark, B. *Computer-Controlled Systems—Theory and Design*; Prentice-Hall: Englewood Cliffs, NJ, USA, 1990.
24. Durgam, R.; Karampuri, R. Modulation Technique to Improve the Performance of a Voltage Controlled Wind Energy Conversion System. In Proceedings of the 2022 Second International Conference on Power, Control and Computing Technologies (ICPC2T), Raipur, India, 1–3 March 2022; pp. 1–6. [[CrossRef](#)]
25. Pande, J.; Nasikkar, P.; Kotecha, K.; Varadarajan, V. A Review of Maximum Power Point Tracking Algorithms for Wind Energy Conversion Systems. *J. Mar. Sci. Eng.* **2021**, *9*, 1187. [[CrossRef](#)]
26. Majout, B.; El Alami, H.; Salime, H.; Zine Laabidine, N.; El Mourabit, Y.; Motahhir, S.; Bouderbala, M.; Karim, M.; Bossoufi, B. A Review on Popular Control Applications in Wind Energy Conversion System Based on Permanent Magnet Generator PMSG. *Energies* **2022**, *15*, 6238. [[CrossRef](#)]
27. Bouderbala, M.; Bossoufi, B.; Lagrioui, A.; Taoussi, M.; Aroussi, H.A.; Ihedrane, Y. Direct and indirect vector control of a doubly fed induction generator based in a wind energy conversion system. *Int. J. Electr. Comput. Eng.* **2019**, *9*, 1531–1540. [[CrossRef](#)]
28. Mahfoud, M.E.L.; Bossoufi, B.; Ouanjli, N.E.L.; Mahfoud, S.; Taoussi, M. Improved Direct Torque Control of Doubly Fed Induction Motor Using Space Vector Modulation. *Int. J. Intell. Eng. Syst.* **2021**, *14*, 177–188. [[CrossRef](#)]
29. Zaihidee, F.M.; Mekhilef, S.; Mubin, M. Robust Speed Control of PMSM Using Sliding Mode Control (SMC)—A Review. *Energies* **2019**, *12*, 1669. [[CrossRef](#)]

30. Taoussi, M.; Bossoufi, B.; Bouderbala, M.; Motahhir, S.; Alkhamash, E.H.; Masud, M.; ZineLabidine, N.; Karim, M. Implementation and Validation of Hybrid Control for Wind Turbine Using FPGA Controller Board. *Electronics* **2021**, *10*, 3154. [[CrossRef](#)]
31. Bouderbala, M.; Bossoufi, B.; Deblecker, O.; Alami Aroussi, H.; Taoussi, M.; Lagrioui, A.; Motahhir, S.; Masud, M.; Alraddady, F.A. Experimental Validation of Predictive Current Control for DFIG: FPGA Implementation. *Electronics* **2021**, *10*, 2670. [[CrossRef](#)]
32. Osman, A.M.; Alsokhry, F. Sliding Mode Control for Grid Integration of Wind Power System Based on Direct Drive PMSG. *IEEE Access* **2022**, *10*, 26567–26579. [[CrossRef](#)]
33. Majout, B.; Abrahmi, D.; Ihedrane, Y.; El Bakkali, C.; Mohammed, K.; Bossoufi, B. Improvement of sliding mode power control applied to wind system based on doubly-fed induction generator. *Int. J. Power Electron. Drive Syst.* **2021**, *12*, 441–452. [[CrossRef](#)]
34. Shen, X.; Liu, J.; Alcaide, A.M.; Yin, Y.; Leon, J.I.; Vazquez, S.; Wu, L.; Franquelo, L.G. Adaptive Second-Order Sliding Mode Control for Grid-Connected NPC Converters with Enhanced Disturbance Rejection. *IEEE Trans. Power Electron.* **2022**, *37*, 206–220. [[CrossRef](#)]
35. Zholtayev, D.; Rubagotti, M.; Do, T.D. Adaptive super-twisting sliding mode control for maximum power point tracking of PMSG-based wind energy conversion systems. *Renew. Energy* **2022**, *183*, 877–889. [[CrossRef](#)]
36. Benbouhenni, H.; Boudjema, Z.; Bizon, N.; Thounthong, P.; Takorabet, N. Direct Power Control Based on Modified Sliding Mode Controller for a Variable-Speed Multi-Rotor Wind Turbine System Using PWM Strategy. *Energies* **2022**, *15*, 3689. [[CrossRef](#)]
37. Bossoufi, B.; Karim, M.; Taoussi, M.; Aroussi, H.A.; Bouderbala, M.; Deblecker, O.; Motahhir, S.; Nayyar, A.; Alzain, M.A. Rooted Tree Optimization for the Backstepping Power Control of a Doubly Fed Induction Generator Wind Turbine: DSPACE Implementation. *IEEE Access* **2021**, *9*, 26512–26522. [[CrossRef](#)]
38. Bouderbala, M.; Bossoufi, B.; Aroussi, H.A.; Taoussi, M.; Lagrioui, A. Novel deadbeat predictive control strategy for DFIG's back to back power converter. *Int. J. Power Electron. Drive Syst.* **2022**, *13*, 2731–2741. [[CrossRef](#)]